Nano Energy 51 (2018) 786–792

Contents lists available at ScienceDirect

Nano Energy

journal homepage: www.elsevier.com/locate/nanoen

Full paper

Engineering active edge sites of fractal-shaped single-layer MoS_2 catalysts for high-efficiency hydrogen evolution

Yi Wan[a,b], Zeyao Zhang[c], Xiaolong Xu[a], Zhihong Zhang[d], Pan Li[a], Xin Fang[a], Kun Zhang[a], Kai Yuan[a], Kaihui Liu[a,b], Guangzhao Ran[a,b], Yan Li[c,*], Yu Ye[a,b,**], Lun Dai[a,b,**]

[a] State Key Lab for Mesoscopic Physics and School of Physics, Peking University, Beijing 100871, PR China
[b] Collaborative Innovation Center of Quantum Matter, Beijing 100871, PR China
[c] Key Laboratory for the Physics and Chemistry of Nanodevices, Beijing National Laboratory of Molecular Sciences, State Key Laboratory of Rare Earth Materials Chemistry and Applications, College of Chemistry and Molecular Engineering, Peking University, Beijing 100871, PR China
[d] Academy for Advanced Interdisciplinary Studies, Peking University, Beijing 100871, PR China

ARTICLE INFO

Keywords:
Hydrogen evolution reaction
Fractal-shaped
Single-layer MoS_2
Active edge site
Electrocatalysis

ABSTRACT

The hydrogen evolution reaction (HER) is a crucial step in electrochemical water splitting that demands an efficient, cheap, and stable catalyst to succeed in practical applications. Two-dimensional (2D) layered molybdenum disulfide (MoS_2), known to contain active edge sites and a chemically inert basal plane, has provided great promise as a non-precious alternative to platinum-based catalysts for electrochemical hydrogen production from water. Here, we directly synthesize fractal-shaped single-layer MoS_2 with large tensile strain on fused silica. The as-synthesized MoS_2 with a large amount of exposed edge sites is superior to the triangle-shaped MoS_2 grown on SiO_2 for catalyzing HER. By controlling the MoS_2 grain size and coverage, etc., we identify the active sites of the MoS_2. Electrocatalytic activity of the MoS_2 for the HER correlates linearly with the number of edge sites with an enhanced activity of $\sim 2.74 \times 10^{-7}$ $\mu A\,\mu m^{-1}$, due to the increased supplying of electrons to the active edge sites caused by the large tensile strain. The optimal HER electrocatalyst of the fractal-shaped single-layer MoS_2, which has an edge-to-substrate ratio of about 0.33 μm^{-1}, exhibits superior HER catalytic activities such as a low overpotential of 185 mV at a current density of 10 $mA\,cm^{-2}$, a Tafel slope of 45 mV/dec, an exchange current density of 50.9 $\mu A\,cm^{-2}$, and long-term stability. The present study provides new ways to design 2D HER electrocatalysts, including controlling the geometry, strain, and modulating the electrical conductivity.

1. Introduction

The quest for highly efficient hydrogen generation has been one of the major driving forces towards future renewable energy production [1–3]. Electrochemical water splitting is a well-known method for hydrogen production, attracting significant attention due to the abundant source and lack of any pollutants [4]. In an efficient hydrogen evolution reaction (HER), catalysts are used to reduce the electrochemical overpotentials. A high-performance HER electrocatalyst should exhibit fast electron transfer, large density of catalytic active sites, and appropriate Gibbs free energy of adsorbed atomic hydrogen. Noble metals, in particular platinum (Pt), is the most effective HER electrocatalyst [3,5]. However, due to its natural scarcity and high cost, it is not suitable for large-scale H_2 production applications. Therefore, it remains challenging to explore earth-abundant electrocatalysts for high-efficiency HER.

Two-dimensional (2D) MoS_2, an earth-abundant material with appropriate Gibbs free energy of adsorbed atomic hydrogen [3,6], has been investigated as a promising electrocatalyst for HER. However, it was found that the HER activity of MoS_2 arises from the active edge sites, as the basal planes are catalytically inert [6]. To produce a more active catalyst, one needs to control the MoS_2 morphology to expose a greater fraction of the catalytically active sites. Many attempts have been made to improve the catalytic activity of MoS_2 by exposing edge sites, such as using nanostructured MoS_2 [7], MoS_2 nanoparticles [8], vertical MoS_2 nanoflakes [9–11], and mesoporous MoS_2 films [12]. However, it is still challenging to directly synthesize edge-abundant MoS_2 flakes since the formation of catalytically active edge sites can be thermodynamically unfavorable compared with the formation of the inert basal plane sites [8].

Herein, we directly synthesize fractal-shaped single-layer MoS_2 with

* Corresponding author.
** Corresponding authors at: State Key Lab for Mesoscopic Physics and School of Physics, Peking University, Beijing 100871, PR China.
E-mail addresses: yanli@pku.edu.cn (Y. Li), ye_yu@pku.edu.cn (Y. Ye), lundai@pku.edu.cn (L. Dai).

https://doi.org/10.1016/j.nanoen.2018.02.027
Received 13 September 2017; Received in revised form 1 February 2018; Accepted 12 February 2018
Available online 15 February 2018
2211-2855/ © 2018 Elsevier Ltd. All rights reserved.

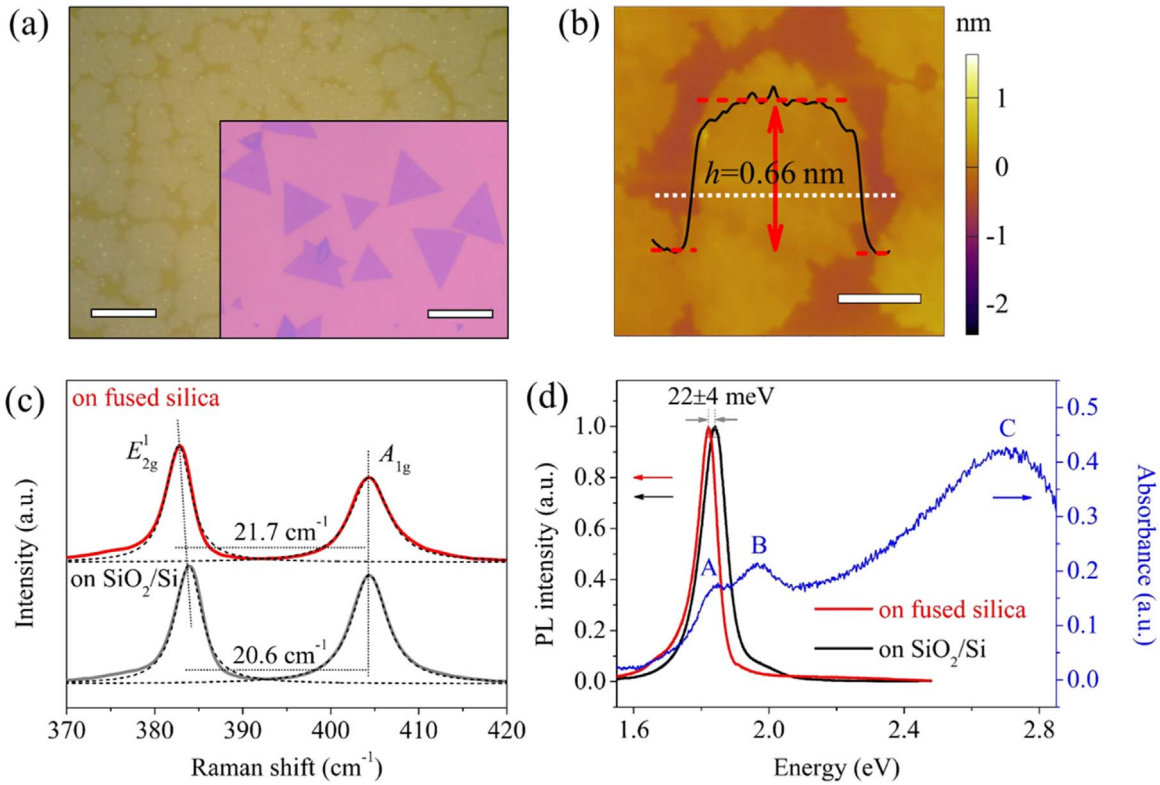

Fig. 1. (a) Optical microscopy image of MoS_2 flakes grown on fused silica. Inset: optical microscopy image of MoS_2 flakes grown on 285 nm SiO_2/Si. Scale bars: 20 μm. (b) AFM topography image of MoS_2 on fused silica with the line profile showing a thickness of ~ 0.66 nm. Scale bar: 2 μm. (c) Raman spectra of single-layer MoS_2 grown on fused silica and on SiO_2/Si. (d) PL spectra obtained from single-layer MoS_2 grown on fused silica and on SiO_2/Si, along with optical absorbance spectrum of single-layer MoS_2 on fused silica.

large tensile strain on fused silica. Due to the abundant active edge sites, the fractal-shaped MoS_2 exhibits enhanced HER catalytic activity. Electrocatalytic HER activity of MoS_2 increases linearly with the number of edge sites. With an edge-to-substrate ratio of 0.33 μm^{-1}, the fractal-shaped MoS_2 shows the superior HER catalytic activity with an operating potential of 185 mV at a current density of 10 mA cm^{-2}, an exchange current density of 50.9 μA cm^{-2}, a Tafel slope of 45 mV/dec, and long-term stability. Moreover, we investigate the importance of electrical coupling between the MoS_2 catalyst and the electrode [13–16] by inserting graphene with different conductivities. This hybrid 2D heterostructure, which combines the pronounced catalytically active MoS_2 edge sites and highly conductive graphene, may provide a promising pathway for developing an efficient HER electrocatalyst.

2. Results and discussion

The fractal-shaped MoS_2 flakes with tortuous edges were synthesized on fused silica substrates via the CVD method (Fig. 1a) [17]. The fractal-shaped flakes remain unchanged in morphology after being transferred to target substrates by a water-soluble polymer-assisted method (see Supporting information Fig. S2a) [18]. The atomic force microscope (AFM) height image of a fractal-shaped MoS_2 flake exhibits a nearly homogeneous color contrast, indicating the uniformity of sample thickness (Fig. 1b), while the line profile across the MoS_2 edges confirms a single-layer thickness of about 0.66 nm [19]. X-ray photoelectron spectroscopy (XPS) is used to investigate the crystal structure of as-prepared MoS_2 on fused silica (see Supporting information Fig. S1), confirming the stoichiometry of the MoS_2 (Mo/S ratio) to be about 1: 1.93.

It is obvious that the fractal-shaped MoS_2 possesses a larger amount of exposed torturous edges, in marked contrast to the triangle-shaped MoS_2 grown on SiO_2/Si substrates (inset of Fig. 1a). Compared to the single-layer triangle-shaped MoS_2, the strain-sensitive in-plane Raman signature (E^1_{2g} mode) of the fractal-shaped MoS_2 red-shifts 1.2 ± 0.5 cm^{-1} (Fig. 1c), showing an enhanced tensile strain of 0.57% [20]. It has been pointed out that this tensile strain may arise from the fast-cooling process from the high growth temperature (650 °C) to room temperature [21]. Due to the fact that the thermal expansion coefficient of fused silica is much smaller than that of MoS_2, the fast-cooling process may create a significant contraction mismatch between the MoS_2 flake and the fused silica, resulting in an enhanced tensile stain of the single-layer MoS_2 grown on fused silica [17]. The negligible peak energy difference (~ 0.1 cm^{-1}) of the doping-sensitive Raman characteristic (A_{1g} mode) between the fractal-shaped MoS_2 and triangle-shaped MoS_2 indicates that the fused silica does not induce extraneous doping to the MoS_2 (Fig. 1c) [18]. It is known that the photoluminescence (PL) of single-layer MoS_2 is very sensitive to the relative strain [21]. The PL spectra of the MoS_2 flakes grown on fused silica and SiO_2/Si are both dominated by the A exciton emission (Fig. 1d). Compared with that of the single-layer triangle-shaped MoS_2 on SiO_2/Si, the A exciton peak energy of the fractal-shaped MoS_2 on fused silica red-shifts ~ 22 meV, showing an enhanced tensile strain of about 0.50% [21], which is consistent with the observation from Raman spectroscopy. After being transferred to the target substrates, the fractal-shaped MoS_2 flakes still have an enhanced ~ 0.52% tensile strain compared with the transferred triangle-shaped MoS_2 flakes (see Supporting information Fig. S2b). From the optical absorption spectrum of the single-layer MoS_2 grown on fused silica (Fig. 1d), the well-known A and B peaks associated with optical absorption by band-edge excitons, as well as the C peak associated with a van Hove singularity of single-layer MoS_2, are clearly observed [22], indicating the high quality of single-layer fractal-shaped MoS_2.

In order to investigate the lattice structure of the fractal-shaped single-layer MoS_2, we employed high-resolution transmission electron microscopy (HRTEM). The fractal-shaped MoS_2 exhibits a periodic triangular packing arrangement of Mo atoms, with crystal lattice spacings

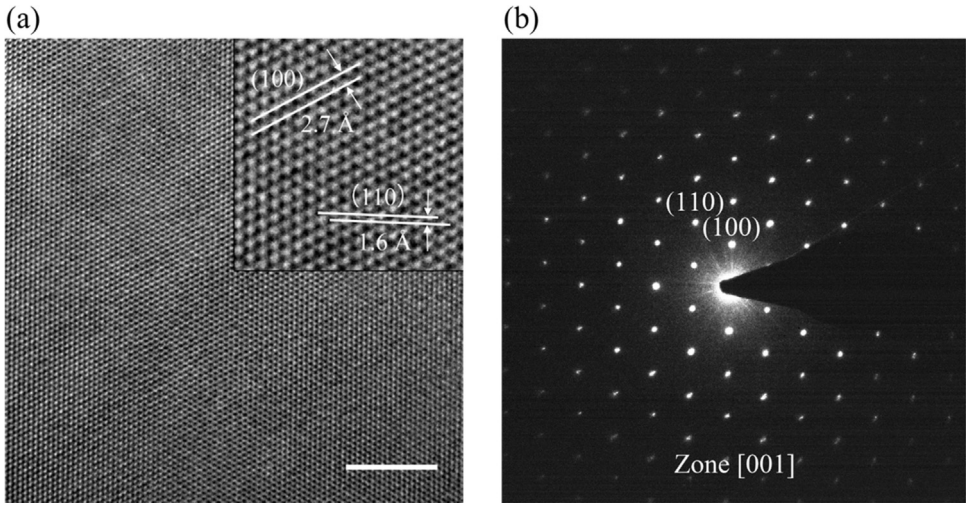

Fig. 2. (a) HRTEM characterization of fractal-shaped single-layer MoS_2. Scale bar: 5 nm. Inset: zoom-in HRTEM image. (b) SAED pattern corresponding to (a).

of 0.27 and 0.16 nm along the (100) and (110) directions, respectively (inset of Fig. 2a). The corresponding selective area electron diffraction (SAED) pattern clearly reveals one set of six-fold symmetry diffraction spots (Fig. 2b), indicating the high crystallinity of the fractal-shaped MoS_2 sample.

Previous theoretical [6] and experimental [8,23–25] studies reveal that the electrocatalytic HER activity correlates with the number of exposed edge sites that have a local stoichiometry, physical structure and electronic structure differing from the catalytically inert basal plane of MoS_2. The unique morphology of the fractal-shaped single-layer MoS_2 greatly increases the edge-to-substrate ratio, which is desired for efficient HER. Moreover, according to *d*-band theory, tensile-strain in MoS_2 could increase the supply of electrons to the catalytic active sites, thereby increasing the electrocatalytic HER activity [26,27].

By modifying the growth conditions, e.g. substrate-to-source distance, we can further control the fractal-shaped MoS_2 coverage and edge-to-surface ratio, where the MoS_2 coverage and the edge-to-surface ratio are defined by $area_{MoS2}/area_{substrate}$ and $perimeter_{MoS2}/area_{MoS2}$, respectively. With increasing the distance between the substrate and the source, the fractal-shaped MoS_2 grain size decreases monotonically, leading to a decreasing area coverage and an increasing edge-to-surface ratio. We label the samples as a, b, c for the substrate-to-source distances of 1.5 cm, 2.0 cm, and 2.5 cm, respectively. From the scanning electron microscopy (SEM) images of samples a to c (Fig. 3a–c), where the black curves in white boxes demarcate the edge profiles of the fractal-shaped single-layer MoS_2 flakes, we can quantitatively extract the area coverage to be about 73.2%, 55.1%, and 36.9%, while the edge-to-surface ratio to be about 0.14 μm^{-1}, 0.45 μm^{-1}, and 0.89 μm^{-1}, respectively. We can extract the edge length parameter, represented by the edge-to-substrate ratio ($perimeter_{MoS2}/area_{substrate}$), to be 0.10 μm^{-1}, 0.25 μm^{-1}, and 0.33 μm^{-1}, respectively, for samples a to c.

In order to elucidate the MoS_2 edge effect for HER, we performed the electrocatalytic HER measurements using fractal-shaped MoS_2 with different edge-to-substrate ratios. To measure HER activity, we transferred the MoS_2 samples a to c from the growth substrates onto glassy carbon (GC) electrodes. Catalytic performance of the samples was measured in a three-electrode system, which is widely used in a typical HER catalytic measurements [28]. Representative linear sweep voltammetry (LSV) for the GC electrode, fractal-shaped MoS_2 (samples a to c) with different edge-to-substrate ratios, and the Pt electrode are plotted in Fig. 3d. Current densities are normalized by the electrode surface area. The featureless polarization curve for a bare GC electrode shows negligible HER activity. In contrast, all three fractal-shaped MoS_2 catalysts show obvious HER activity. To rule out the possibility Pt counter electrode-induced enhanced HER performance, we conduct the electrochemical measurement of the identical MoS_2 sample by using Pt and carbon rods as counter electrodes (see Supporting information Fig. S3b). The two LSV curves nearly overlap with each other and no clear change appears in the current densities by using either a Pt or a carbon counter electrode.

The operating potentials (η) of MoS_2 samples a, b, and c at the current density of 10 mA cm^{-2} are 605 mV, 453 mV and 185 mV, respectively, versus the reversible hydrogen electrode (RHE) (Fig. 3d). It is worth noting that, at the same potential, the MoS_2 samples with higher coverage (samples a and b) exhibit smaller current density and much lower catalytic activity compared with the MoS_2 sample with smaller coverage (sample c), indicating that the surface coverage is less important for the catalytic activity. On the contrary, the MoS_2 edge length plays an important role in enhancing the catalytic activity. As shown in Fig. 4a, it is obvious that the Tafel slope of sample c (45 mV/dec) is smaller than those of samples a (233 mV/dec) and b (118 mV/dec). The Tafel slope is an inherent property of the catalyst that is determined by the rate-limiting step of the HER. The observed Tafel slope of ~ 45 mV/dec, which is one of the lowest values reported for MoS_2-based catalysts (Fig. 4b), suggests that electrochemical desorption is the rate-limiting step, and thus the Volmer-Heyrovsky mechanism dominates in the HER catalyzed by the fractal-shaped MoS_2. For reference, the HER on a Pt surface, with a small Tafel slope of 30 mV/dec and a large exchange current density of 511.7 μA cm^{-2}, is known to work based on the Volmer-Tafel mechanism and the recombination step is the rate-limiting step.

Another important criterion for HER activity is the exchange current density (j_0), which can be obtained by applying linear extrapolation of Tafel plots based on the Tafel equation, $\eta = a \times \log(j/j_0)$, where a represents Tafel slope (Fig. 3e). Exchange current density reflects the intrinsic rate of electron transfer between an analyte and the electrode. We can see that MoS_2 sample c, with the largest edge-to-substrate ratio of 0.33 μm^{-1}, displays the highest exchange current density of 50.9 μA cm^{-2}, which is one of the highest values among those reported for MoS_2-based catalysts [29]. As shown in Fig. 4a, the exchange current density j_0 linearly correlates with the edge-to-substrate ratio, with a slope of ~ 2.74×10^{-7} μA μm^{-1}. The observed exchange current density per edge length is much higher than the reported values for MoS_2-based catalysts [6,30–33], which may result from the increased supply of electrons to the active edge sites caused by the large tensile strain of the fractal-shaped single-layer MoS_2 [26,27].

This hypothesis is confirmed by electrochemical impedance spectroscopy (EIS) and electrochemical active surface area (ECSA). EIS is a

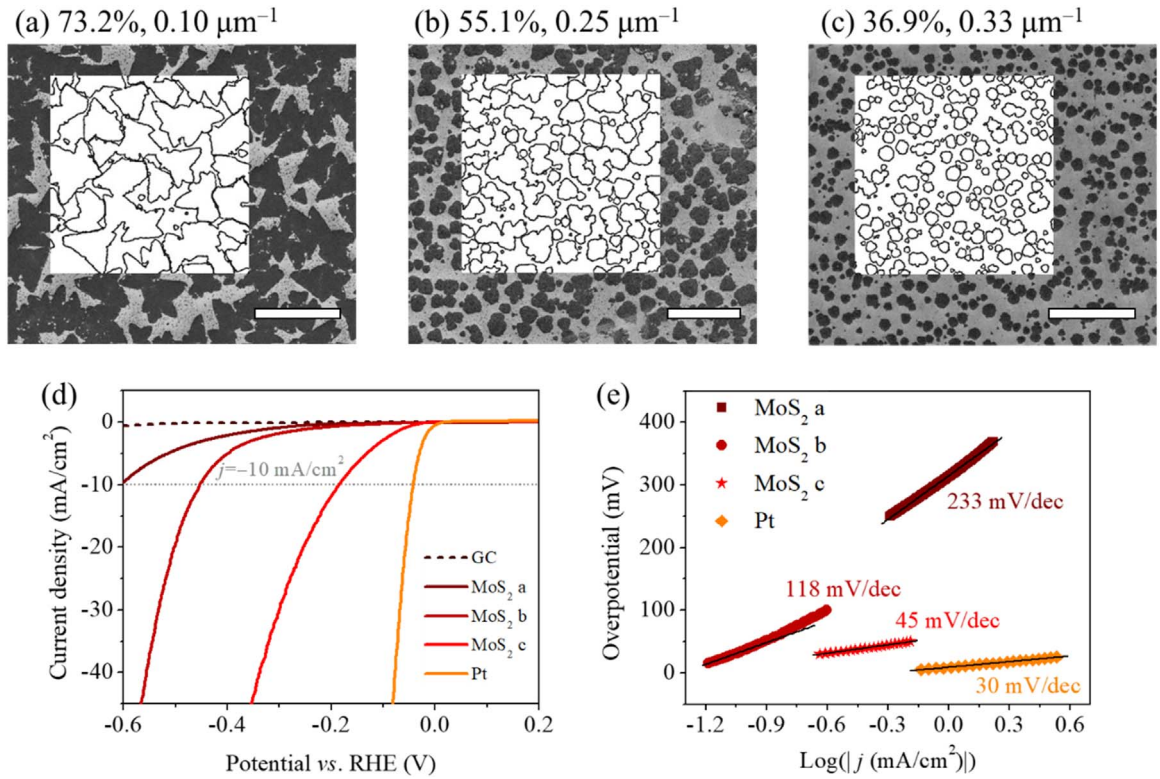

Fig. 3. (a)–(c) SEM images of different MoS_2 samples grown on fused silica. The samples exhibit the typical fractal morphology with tortuous edges but with different area coverage (%) and edge-to-substrate ratio (μm^{-1}). Scale bar: 50 μm. The line profiles (the black curves in white boxes) for the MoS_2 samples are extracted from the SEM images with the assistance of Image J software. (d) Polarization curves in a cathodic potential window for the three different MoS_2 samples a-c, as well as a blank GC electrode without the catalyst decoration and a Pt foil for references. (e) Corresponding Tafel plots (overpotential *vs.* log current density).

useful technique to characterize interface reactions and electrode kinetics in HER (see Supporting information Fig. S4). The representative Nyquist plots of MoS_2 a–c all exhibit one semicircle at a fixed overpotential of 300 mV (Fig. 4b), indicating that the corresponding equivalent circuit for the HER (inset of Fig. 4b) can be characterized by one time constant. The charge transfer resistance (R_{ct}) represents the electrocatalysis kinetics at the electrode-electrolyte interface, with a smaller value corresponding to a faster reaction rate. By fitting to the corresponding equivalent circuit for the Nyquist plots, we can obtain a much smaller charge transfer resistance for the MoS_2 c (305 Ω), compared to those of the MoS_2 a (1967 Ω) and b (1365 Ω). This further demonstrates that the rapid carrier transportation between the catalytic edge sites of MoS_2 and the electrode substrate plays an important role in enhancing the HER performance. The other reason for the excellent HER performance of the MoS_2 c is the large effective electrochemically active area, which could be estimated by electrochemical double-layer capacitance (C_{dl}) (see Supporting information Fig. S5). The measured capacitive current densities in a potential range under non-Faradic condition show linear dependences with the scan rate, determining the specific capacitances of 0.03, 0.29 and 1.30 mF/cm^2 for MoS_2 a, b and c, respectively. Thus, the calculated electrochemical active surface areas are 0.75, 7.25 and 32.5 cm^2_{ECSA} for MoS_2 a, b and c, respectively. Besides, after a continuous HER operation, the morphology and crystalline property of MoS_2 samples are examined (see Supporting information Fig. S6). Despite there exists some damage to the sample morphology, the high crystallinity of the fractal-shaped MoS_2 sample remains even after a long-time continuous operation. The XPS spectra before and after electrochemical treatment can only be well fitted by singular 2H-MoS_2 components, indicating no obvious MoS_2 phase transition from semiconducting phase (2 H) to metallic phase (1 T) occur during the electrochemical reaction [34,35].

To further enhance the catalytic activity of the MoS_2 catalyst, we manage to modulate the electrical coupling between the MoS_2 and the electrode to increase the electron transport [13,14,36] by inserting a graphene to form a van der Waals heterostructure with MoS_2, as shown in Fig. 5a. Single-layer graphene samples with different conductivities (see supporting information S8), named as graphene I and graphene II, were used. The room-temperature Hall sheet resistances of graphene I and II are about 861 ± 17 Ω/□ and 476 ± 3 Ω/□, respectively. The catalytically inert single-layer graphene (coverage ≥ 97%) and catalytically active single-layer MoS_2 (coverage ~ 34.8%, edge-to-substrate ratio ~ 0.31 μm^{-1}) were successively transferred onto the top of the GC electrode (Fig. 5b). The graphene I (II)-supported MoS_2 catalyst exhibits an operating potential of 303 mV (198 mV) at the current density of 10 mA cm^{-2}, and a Tafel slope of 81 mV/dec (69 mV/dec) (Fig. 5b and c). The higher electrocatalytic performance for graphene II-supported MoS_2 may result from the higher conductivity. It is reasonable to believe that the HER performance can be further improved by modifying the substrate conductivity, such as converting a portion of the 2H-MoS_2 to 1T-MoS_2 or employing MoS_xSe_{2-x} alloy to substitute MoS_2. Finally, we evaluate the long-cycle stability of the catalysts, which is an important indicator for electrochemical practical application, using a long-term cycling test in a 0.5 M aqueous H_2SO_4 solution. Here, the result for Graphene II-support MoS_2 is presented (Fig. 5d) as a representative. After 1000 cyclic voltammetry (CV) cycles, the electrochemical performance does not show any obvious degradation, showing the excellent long-term electrochemical stability.

3. Conclusions

In summary, we have synthesized single-layer fractal-shaped MoS_2 flakes with a large tensile strain and abundant active edge sites, and used them as catalysts for the electrochemical HER. Electrochemical HER activity increases linearly with the number of edge sites on the MoS_2 catalyst with an enhanced activity of ~ 2.74×10^{-7} μA μm^{-1}. The optimal MoS_2 catalyst shows an overall high HER catalytic

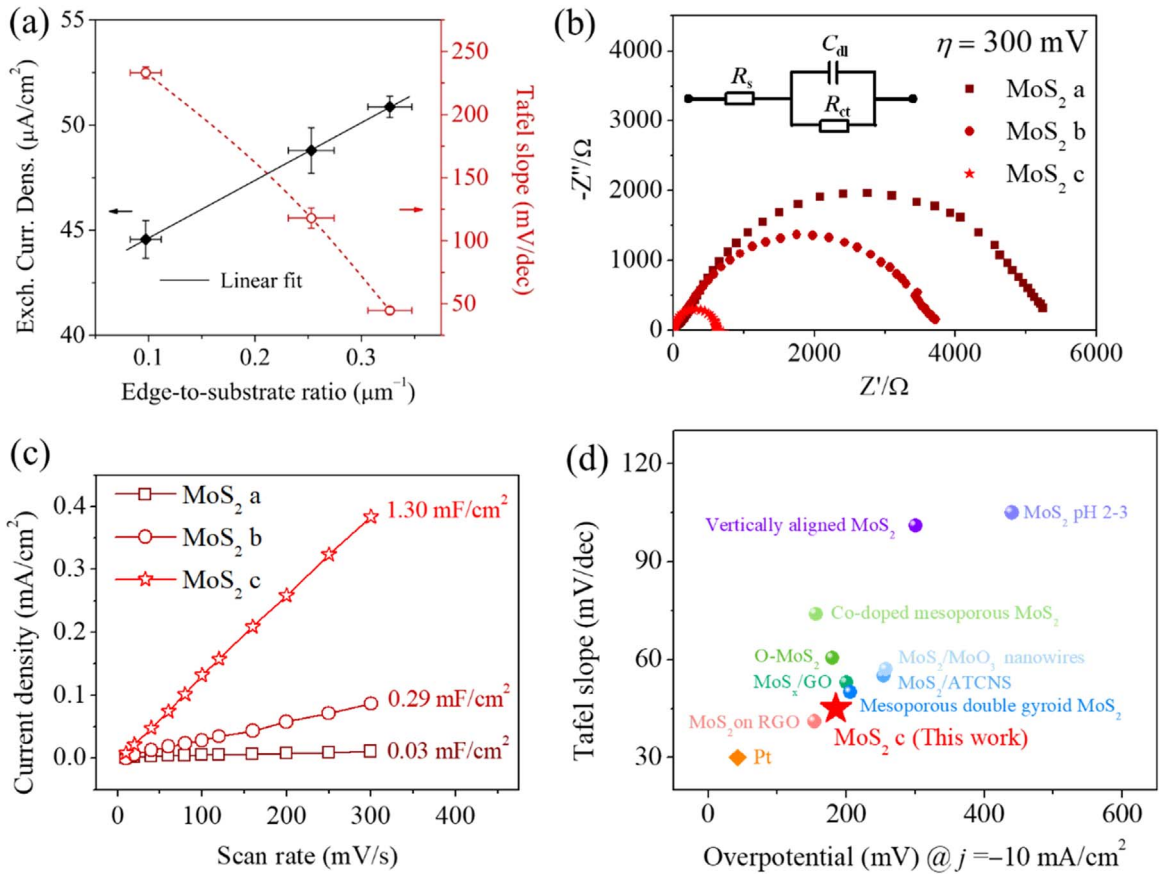

Fig. 4. (a) Exchange current density and Tafel slope versus MoS_2 edge-to-substrate ratio, where the exchange current density shows a linear dependence of edge-to-substrate ratio. (b) EIS of GC electrodes modified with MoS_2 a-c at overpotential of 300 mV. Inset: Equivalent electrical circuit used to model the HER process. (c) The measured capacitive currents plotted as a function of scan rate. The specific capacitances obtained from the slope of linear fitting are 0.03, 0.29 and 1.30 mF/cm^2 for MoS_2 a, b and c, respectively. (d) The HER performances of the fractal-shaped single-layer MoS_2 (sample c) and Pt foil measured in this work, including two important parameters, overpotential η (mV *vs.* RHE) when $j = -10$ mA/cm^2 and Tafel slope. The performances of the reported MoS_2-based catalysts for HER are summarized for comparison [7–16].

activities, including a low operating potential of 185 mV at current density of 10 mA cm^{-2}, a large exchange current density of 50.9 μA cm^{-2}, and a low Tafel slope of 45 mV/dec, which are among the best reported values of MoS_2-based electrocatalysts so far. We also expect to enhance the HER activity by increasing the electrical coupling between the MoS_2 catalyst and the electrode through inserting higher-conductivity graphene or other thin layer material in future. Our findings here deepen the understanding of the effect of abundant active sites, strain and electrical transfer on the high-efficiency HER performance of MoS_2-based electrocatalysts. We believe this work could be a significant advance towards the batch production and electrocatalytic applications of 2D materials, and hope these results will motivate scientists to explore new efficient catalysts in the large 2D materials family for energy related applications.

4. Experimental section

4.1. Sample preparation and transfer

Fractal-shaped single-layer MoS_2 was grown via a CVD method in a dual-temperature-zone system using S and MoO_3 as precursors, fused silica as substrates, and high-purity Ar as carrier gas. S powder, MoO_3 powder, and the substrates were placed in sequence from upstream to downstream of the carrier gas flow direction. The temperatures for S and MoO_3 sources were elevated from room temperature to 160 and 650 °C, respectively, in 40 min, and kept at 650 °C, for 5 min, followed by a natural cooling process. During the whole process, the argon flow rate was kept at 15 sccm.

To transfer the large-area single-layer MoS_2 flakes, 0.75 g of polyvinylpyrrolidone (PVP), 1.5 mL of *N*-vinylpyrrolidone (NVP), and 0.75 mL of deionized water were dissolved in ethanol to prepare 10 mL solution. A few drops of the solution were then spin-coated on the growth substrate covered by single-layer MoS_2 flakes at 2500 rpm for 1 min, followed by a baking at 70 °C for 1 min to remove the solvents. To enhance the strength of the polymer mediator, 9 wt% poly(vinyl alcohol) (PVA) aqueous solution was spin-coated on it, and these two water-soluble polymers integrated into a solid film after being baked in the same condition as above. The polymer, together with the MoS_2, samples can be peeled off slowly from the growth substrate by tweezers, and transferred onto the target substrate. The polymer adheres to the substrate through an electrostatic force. Finally, the polymer was removed by soaking in deionized water of 80 °C for 2 h, and single-layer MoS_2 flakes were left on the target substrate without damage.

4.2. Characterization of single-layer MoS_2

Optical microscopy (Zeiss Axio Imager, A2m) equipped with a white light source (Zeiss Hal 100, 100 W), a charge-coupled device (CCD) camera, and a spectrometer (Andor, Shamrock 500i), PL and Raman spectroscopy (Horiba, Labram HR800), AFM (Cypher S, Asylum Research), SEM (FEI NanoSEM 430) and TEM (FEI Tecnai F30) were used to characterize the samples.

4.3. Electrochemical measurements

Electrochemical measurements were performed at room

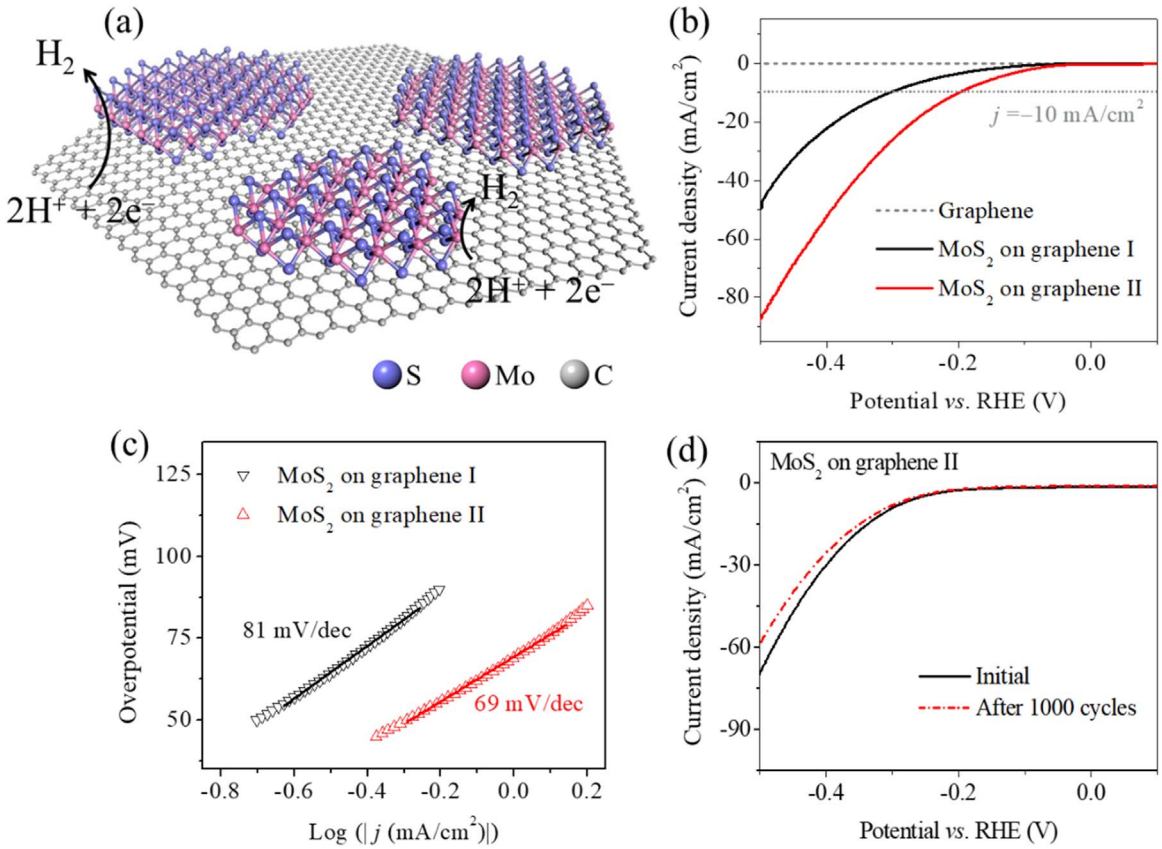

Fig. 5. (a) Schematic illustration of the heterostructure combining single-layer fractal-shaped MoS_2 and single-layer graphene. (b) Polarization curves for the two heterostructures, as well as a GC electrode decorated only with single-layer graphene. (c) Corresponding Tafel plots. (d) Stability test of MoS_2/graphene II. The polarization curves are recorded before and after 1000 potential cycles in 0.5 M H_2SO_4 solution from 0.2 to − 0.7 V (*vs.* RHE).

temperature using a transferred MoS_2-decorated GC electrode (5 mm diameter, 0.196 cm^2) as the working electrode in a three-electrode system on an electrochemical workstation (CHI760E). The GC electrode was polished to a mirror finish and thoroughly cleaned before use. A Pt rod (or a carbon rod) and saturated Ag/AgCl were used as counter and reference electrodes, respectively. All the potentials were calibrated to the RHE. Before the electrochemical measurement, the electrolyte (0.5 M H_2SO_4) was degassed by bubbling pure N_2 for 30 min to ensure the saturation of the electrolyte. The polarization curves were obtained by LSV with a scan rate of 25 mV/s and a rotating speed of 1600 rpm throughout the measurement in order to remove in situ H_2 bubbles.

Acknowledgments

This work was supported by the National Basic Research Program of China (No. 2013CB921901), National Key R&D Program of China (Nos. 2017YFA0206301 and 2016YFA0300903), Beijing Natural Science Foundation (4182028), National Natural Science Foundation of China (Nos. 61521004, 11474007 and 51522201), and Ministry of Science and Technology of China (No. 2016YFA0201904).

Notes

The authors declare no competing financial interest.

Appendix A. Supporting information

Supplementary data associated with this article can be found in the online version at http://dx.doi.org/10.1016/j.nanoen.2018.02.027.

References

[1] M.S. Dresselhaus, I.L. Thomas, Nature 414 (6861) (2001) 332–337.
[2] J.A. Turner, Science 305 (5686) (2004) 972–974.
[3] J.K. Norskov, C.H. Christensen, Science 312 (5778) (2006) 1322–1323.
[4] G.W. Crabtree, M.S. Dresselhaus, M.V. Buchanan, Phys. Today 57 (12) (2004) 39–44.
[5] J. Greeley, T.F. Jaramillo, J. Bonde, I. Chorkendorff, J.K. Norskov, Nat. Mater. 5 (11) (2006) 909–913.
[6] T.F. Jaramillo, K.P. Jørgensen, J. Bonde, J.H. Nielsen, S. Horch, I. Chorkendorff, Science 317 (5834) (2007) 100–102.
[7] J.D. Benck, Z. Chen, L.Y. Kuritzky, A.J. Forman, T.F. Jaramillo, ACS Catal. 2 (9) (2012) 1916–1923.
[8] J. Kibsgaard, Z. Chen, B.N. Reinecke, T.F. Jaramillo, Nat. Mater. 11 (11) (2012) 963.
[9] D. Kong, H. Wang, J.J. Cha, M. Pasta, K.J. Koski, J. Yao, Y. Cui, Nano Lett. 13 (3) (2013) 1341–1347.
[10] Wen-Hui Hu, Guan-Qun Han, Fang-Na Dai, Yan-Ru Liu, Xiao Shang, Bin Dong, Yong-Ming Chai, Yun-Qi Liu, Chen-Guang Liu, Int. J. Hydrog. Energy 41 (2016) 294–299.
[11] Xiao Shanga, Wen-Hui Hua, Xiao Lia, Bin Dong, Yan-Ru Liua, Guan-Qun Hana,b, Yong-Ming Chaia, Chen-Guang Liua, Electrochim. Acta 224 (2017) 25–31.
[12] J. Deng, H. Li, S. Wang, D. Ding, M. Chen, C. Liu, Z. Tian, K.S. Novoselov, C. Ma, D. Deng, X. Bao, Nat. Commun. 8 (2017) 14430.
[13] Z. Chen, D. Cummins, B.N. Reinecke, E. Clark, M.K. Sunkara, T.F. Jaramillo, Nano Lett. 11 (10) (2011) 4168–4175.
[14] Y. Li, H. Wang, L. Xie, Y. Liang, G. Hong, H. Dai, J. Am. Chem. Soc. 133 (19) (2011) 7296–7299.
[15] Wen-Hui Hu, Guan-Qun Han, Yan-Ru Liu, Bin Dong, Yong-Ming Chai, Yun-Qi Liu, Chen-Guang Liu, Int. J. Hydrog. Energy 40 (2015) 6552–6558.
[16] Wen-Hui Hu, Xiao Shang, Guan-Qun Han, Bin Dong, Yan-Ru Liu, Xiao Li, Yong-Ming Chai, Yun-Qi Liu, Chen-Guang Liu, Carbon 100 (2016) 236–242.
[17] Y. Wan, H. Zhang, K. Zhang, Y. Wang, B. Sheng, X. Wang, L. Dai, ACS Appl. Mater. Interfaces 8 (28) (2016) 18570–18576.
[18] Z. Lu, L. Sun, G. Xu, J. Zheng, Q. Zhang, J. Wang, L. Jiao, ACS Nano 10 (5) (2016) 5237–5242.
[19] Y.H. Lee, X.Q. Zhang, W. Zhang, M.T. Chang, C.T. Lin, K.D. Chang, Y.C. Yu, J.T. Wang, C.S. Chang, L.J. Li, T.W. Lin, Adv. Mater. 24 (17) (2012) 2320–2325.
[20] C. Rice, R.J. Young, R. Zan, U. Bangert, D. Wolverson, T. Georgiou, R. Jalil, K.S. Novoselov, Phys. Rev. B 87 (8) (2013).

[21] Z. Liu, M. Amani, S. Najmaei, Q. Xu, X. Zou, W. Zhou, T. Yu, C. Qiu, A.G. Birdwell, F.J. Crowne, R. Vajtai, B.I. Yakobson, Z. Xia, M. Dubey, P.M. Ajayan, J. Lou, Nat. Commun. 5 (2014) 5246.
[22] D. Dumcenco, D. Ovchinnikov, K. Marinov, M. Gibertini, N. Marzari, O.L. Sanchez, Y.C. Kung, D. Krasnozhon, M.W. Chen, S. Bertolazzi, ACS Nano 9 (4) (2015) 4611–4620.
[23] J. Bonde, P.G. Moses, T.F. Jaramillo, J.K. Nørskov, I. Chorkendorff, Faraday Discuss. 140 (1) (2008) 219.
[24] S.M. Tan, A. Ambrosi, Z. Sofer, Š. Huber, D. Sedmidubský, M. Pumera, Chem. – Eur. J. 21 (19) (2015) 7170–7178.
[25] R. Gusmao, Z. Sofer, M. Novacek, J. Luxa, S. Matejkova, M. Pumera, Nanoscale 8 (12) (2016) 6700–6711.
[26] J.H. Lee, W.S. Jang, S.W. Han, H.K. Baik, Langmuir 30 (32) (2014) 9866–9873.
[27] H. Li, C. Tsai, A.L. Koh, L. Cai, A.W. Contryman, A.H. Fragapane, J. Zhao, H.S. Han, H.C. Manoharan, F. Abild-Pedersen, J.K. Norskov, X. Zheng, Nat. Mater. 15 (3) (2016) 364.
[28] B. Guo, K. Yu, H. Li, R. Qi, Y. Zhang, H. Song, Z. Tang, Z. Zhu, M. Chen, ACS Appl. Mater. Interfaces 9 (4) (2017) 3653–3660.
[29] J.D. Benck, T.R. Hellstern, J. Kibsgaard, P. Chakthranont, T.F. Jaramillo, ACS Catal. 4 (11) (2014) 3957–3971.
[30] J. Shi, D. Ma, G.F. Han, Y. Zhang, Q. Ji, T. Gao, J. Sun, X. Song, C. Li, Y. Zhang, ACS Nano 8 (10) (2014) 10196–10204.
[31] L. Wang, Z. Sofer, J. Luxa, M. Pumera, Adv. Mater. Interfaces 2 (9) (2015) 1500041.
[32] X. Chia, A. Adriano, P. Lazar, Z. Sofer, J. Luxa, M. Pumera, Adv. Funct. Mater. 26 (24) (2016) 4306–4318.
[33] X. Chia, A. Ambrosi, P. Lazar, Z. Sofer, M. Pumera, J. Mater. Chem. A 4 (37) (2016) 14241–14253.
[34] R. Kappera, D. Voiry, S.E. Yalcin, B. Branch, G. Gupta, A.D. Mohite, M. Chhowalla, Nat. Mater. 13 (2014) 1128.
[35] X. Chia, A. Ambrosi, D. Sedmidubský, Z. Sofer, M. Pumera, Chem. – Eur. J. 20 (52) (2014) 17426–17432.
[36] M.A. Lukowski, A.S. Daniel, F. Meng, A. Forticaux, L. Li, S. Jin, J. Am. Chem. Soc. 135 (28) (2013) 10274–10277.